

Motion Basis Learning for Unsupervised Deep Homography Estimation with Subspace Projection

Nianjin Ye¹ Chuan Wang¹ Haoqiang Fan¹ Shuaicheng Liu^{2,1}

¹Megvii Technology

²University of Electronic Science and Technology of China

Abstract

In this paper, we introduce a new framework for unsupervised deep homography estimation. Our contributions are 3 folds. First, unlike previous methods that regress 4 offsets for a homography, we propose a homography flow representation, which can be estimated by a weighted sum of 8 pre-defined homography flow bases. Second, considering a homography contains 8 Degree-of-Freedom (DOFs) that is much less than the rank of the network features, we propose a Low Rank Representation (LRR) block that reduces the feature rank, so that features corresponding to the dominant motions are retained while others are rejected. Last, we propose a Feature Identity Loss (FIL) to enforce the learned image feature warp-equivariant, meaning that the result should be identical if the order of warp operation and feature extraction is swapped. With this constraint, the unsupervised optimization is achieved more effectively and more stable features are learned. Extensive experiments are conducted to demonstrate the effectiveness of all the newly proposed components, and results show our approach outperforms the state-of-the-art on the homography benchmark datasets both qualitatively and quantitatively.

1. Introduction

Homography is a fundamental yet important image alignment model that has been widely used for image registration [1]. A homography is a 3×3 matrix that contains 8 Degree-of-Freedom (DOFs), with each 2 for scale, translation, rotation and perspective [9]. Traditionally, a homography is often estimated by detecting and matching image features [16, 19], and then solving a Direct Linear Transform (DLT) [9] with outlier removal [7]. In contrast, deep homography methods take two images as the network input, and directly output a homography matrix [5]. Compared with traditional methods that highly rely on the extracted feature matches, deep methods are more robust against tex-

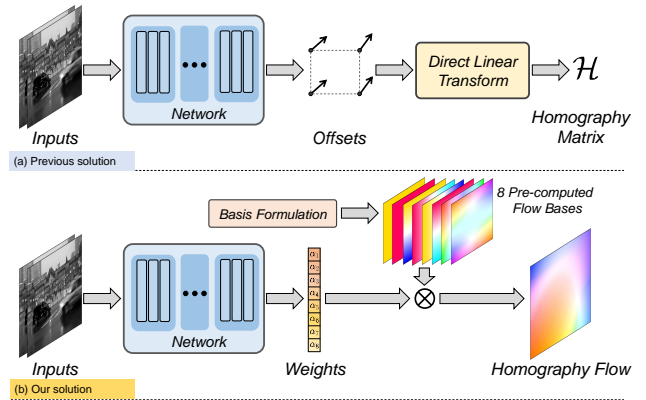


Figure 1. (a) Previous deep homography methods estimate 4 motion offsets and solve a DLT for the result. (b) We construct 8 flow motion basis by modifying matrix elements of a homography, and then regress 8 weights to combine the flow basis for the result.

tureless scenarios.

Deep methods can be classified into two categories, supervised [5, 14] and unsupervised [27, 18]. The former one adopts synthesized examples with ground-truth labels to train the network while the latter one directly minimizes the photometric or feature differences between two images. As synthesized examples cannot reflect scene parallax and dynamic objects, unsupervised methods often generalize better than the supervised ones. For unsupervised methods, Nguyen *et al.* [18] minimized error over the entire image while Zhang *et al.* [27] proposed to learn a mask to skip outlier regions during minimization.

It is not optimal to directly regress the elements of a homography matrix, as they are with different magnitudes. Current solution is to regress 4 offsets [5, 14, 27, 18], which is equivalent to a homography if feeds them to the DLT solver (Fig. 1(a)). In this work, we start from a new direction by proposing a “homography flow” representation (Fig. 1(b)). Specifically, we first generate 8 flow bases by modifying the entries of a homography matrix one at a time. As such, 8 homography matrices are obtained, each

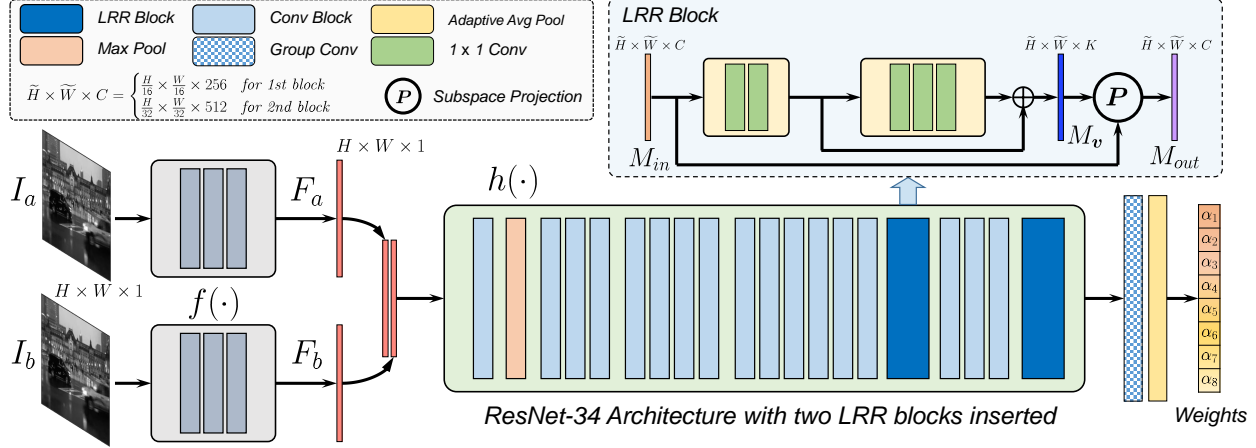


Figure 2. Our network pipeline takes grayscale image patches I_a and I_b as input, and produces 8 weights to combine 8 pre-defined homography bases to produce a homography flow as output. The network consists of two modules, a warp-equivariant feature extractor $f(\cdot)$ and a homography estimator $h(\cdot)$, with 2 inserted LRR blocks to reduce the rank of the motion features.

of which can be further translated into a flow map given the image coordinates, yielding 8 homography flow bases. In **small-baseline** scenarios, a homography flow can be reconstructed inside the space spanned by these flow bases by learning combinational weights.

As homography has only 8 DOFs, the homography flow lies in a low-rank subspace. However, the rank of the motion features through a network are usually much higher than that of a homography. From this observation, we propose to decrease the rank of the features by projecting them into their subspaces. Specifically, the projection contains two steps, including discovering the subspace bases of the features maps and then transforming feature maps into the subspace. To achieve this projection, we propose a Low Rank Representation (**LRR**) block, that can be plugged into a normal CNN and be trained end-to-end for the feature rank reduction. When the rank is reduced, features corresponding to the dominant motions, *i.e.* motions that could be described by a homography, are often retained. Features induced from non-dominant motions, *e.g.*, multi-depth and dynamic contents, are often removed or suppressed.

Besides, it is observed that the feature warp-equivariance cannot be well preserved during the unsupervised training of the previous methods, while this property should have held ideally, *i.e.* $f(\mathcal{W}(I)) = \mathcal{W}(f(I))$, where $\mathcal{W}, f(\cdot)$ represent the warp operation and feature extraction. To this end, we propose a “Feature Identity Loss” (**FIL**) to enforce the image feature warp-equivariant. It is demonstrated that with FIL, the unsupervised optimization can be achieved more effectively and more stable features are learned.

We demonstrate the effectiveness of all the newly proposed techniques and components by extensive experiments and ablation studies. The experimental results also verify that our method outperforms the state-of-the-arts on the

public benchmark both qualitatively and quantitatively. To sum up, our contributions are as follows,

- We propose a new representation “homography flow” that assembles 8 pre-computed flow bases for unsupervised deep homography estimation.
- We propose a new LRR block that reduces motion feature rank so as to reject motion noises implicitly and effectively.
- We propose a new FIL loss that enforces the warp-equivariance of the learned image feature to facilitate a stable unsupervised optimization.

2. Related works

Traditional homography. A homography is often estimated by first detecting and matching image features, such as SIFT [16], ORB [19], SURF [3], LPM [17], GMS [4], SOSNet [23], LIFT [25], BEBLID [21] and OAN [26], after which two sets of point correspondences were established. Next, the false matches were rejected by RANSAC [7], IRLS [11], MAGSAC [2]. Finally, a Direct Linear Transform (DLT) is solved for the homography [8]. Some deep approaches have been proposed for improved feature detection, *e.g.*, SuperPoint [6] or matching, *e.g.*, SuperGlue [20].

Deep homography. The deep homography can be classified into supervised [5, 14] and unsupervised [18, 27] methods. The network takes the source and target images as inputs, and output 4 offsets, so as to produce the homography. In supervised approaches, the two input images are generated from one image with a known homography perturbation. The homography is then, used as the guidance for the training. However, the synthesized images are lack of depth disparities. To overcome such issue, unsupervised approaches directly minimize the photometric loss between

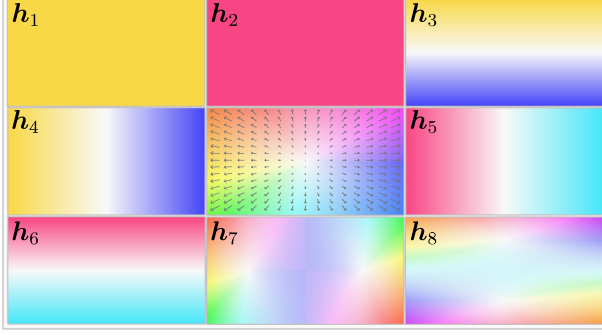


Figure 3. The visualization of the pre-computed 8 orthogonal and normalized flow bases $h_1 \sim h_8$ and the flow legend in the center.

two images, with Spatial Transform Network (STN) [12] to warp the source to the target. Nguyen *et al* [18] minimizes the photometric loss on the entire image while Zhang *et al.* [27] learns a mask to skip outlier regions. In this work, we introduce a novel representation of homography flow, where we learn homography basis instead of offsets.

Basis learning. Our method is also related to basis learning [15]. Tang *et al.* shows that low-level vision problems exist subspaces that can be exploited for the regularization [22]. PCAFlow learns flow basis from movies, showing that the flow estimation can be converted into the learning of the weighted sum of the learned flow bases [24]. Inspired from these works, we learn the coefficients to combine 8 pre-defined flow bases to estimate a homography flow.

3. Algorithm

3.1. Network Structure

Our method is built on convolutional neural networks, which takes two gray image patches I_a and I_b of size $H \times W$ as input, and produces a homography flow H_{ab} from I_a to I_b of the same size as output. The entire structure consists of two modules, a warp-equivariant feature extractor $f(\cdot)$ and a homography estimator $h(\cdot)$. $f(\cdot)$ is a fully convolutional network which accepts input of arbitrary sizes, and $h(\cdot)$ adapts a backbone of ResNet-34 [10] with our newly introduced LRR blocks and produces 8 weights, which are used to linearly combine 8 pre-computed flow bases to obtain H_{ab} . Fig. 2 illustrates the network structure.

Homography flow and its basis formulation. A homography matrix has 8 DOFs and it is computed by solving a Direct Linear Transformation problem after 4 corner offsets of an image are predicted as in [27, 18]. In this paper, we solve the problem from a new perspective. Specifically, our network learns a special optical flow of size $H \times W \times 2$ for small-baseline scenes constrained by homography transformation, called “homography flow”. Due to the constraint, homography flow falls into a 8-D subspace within the entire $2HW$ -D space of a general optical flow. It can be represented by 8 orthogonal flow bases spanning the subspace,

i.e.

$$\exists \{h_i\} \text{ s.t. } h_{ab} = \sum_i \alpha_i h_i \quad (i = 1, 2, \dots, 8) \quad (1)$$

where $h_i \in \mathbb{R}^{2HW}$, $h_i^T h_j = 0$

Here h_{ab} is the flattened version of H_{ab} , and $\{\alpha_i\}$ are the coefficients for the flow bases.

To obtain the orthogonal flow bases, we first generate 8 homography matrix by modifying each single entry h_i of an identity homography matrix, except the entry at the position of (3, 3) which is always normalized to 1. Given the image coordinates, a homography matrix can be converted to a flow map by transforming the image coordinates and minus their original positions. Then, 8 homography flows are normalized by its largest flow magnitude followed by a QR decomposition. Mathematically, it is described as,

$$M = Q \cdot R \quad (M, Q \in \mathbb{R}^{2HW \times 8}, R \in \mathbb{R}^{8 \times 8}) \quad (2)$$

where each column of matrix M is the flattened normalized homography flow H_i as mentioned above. By QR decomposition, columns of Q are orthogonal and they naturally serve as the flow bases spanning the homography subspace, *i.e.* $Q = [h_1, h_2, \dots, h_8]$. In other words, each flow basis is associated with a tangent space at the origin of the homography group. With the 8 bases formulated, a homography flow can be acquired by accurately predicting their weights $\{\alpha_i\}$. Considering the perspective transformation can be approximated well with linear model in small baseline tasks, we can use such a linear-weighted solution to approximate homography. We visualize the bases in Fig. 3.

Warp-equivariant feature extractor. Before [27], previous unsupervised DNN based methods commonly minimize the pixel intensity values for the registration. In [27], the authors proposed to minimize the difference of learned deep features instead of using the original images. In this paper, we similarly follow the idea of [27], but constrain the learned features with warp-equivariance, which means the results should be identical if we swap the order of warp operation \mathcal{W} and feature extraction f given an input image I , *i.e.* $\mathcal{W}(f(I)) = f(\mathcal{W}(I))$. For inputs I_a and I_b , the feature extractor shares weights and produces feature maps F_a and F_b . In practice, features with absolute warp-equivariance are rarely achieved. Thus we introduce a new loss $L_W = |\mathcal{W}(f(I)) - f(\mathcal{W}(I))|$ as a constraint to approximate this property, which is detailed in Sec. 3.3.

Homography estimator with LRR blocks. Given the feature maps F_a and F_b , we concatenate them to build a feature map $[F_a, F_b]$. Then, it is fed to the homography estimator network to produce 8 weights. These weights linearly combine $\{h_i\}$ to produce the final homography flow H_{ab} . We use $h(\cdot)$ to represent the whole process, *i.e.*

$$H_{ab} = h([F_a, F_b]) \quad (3)$$

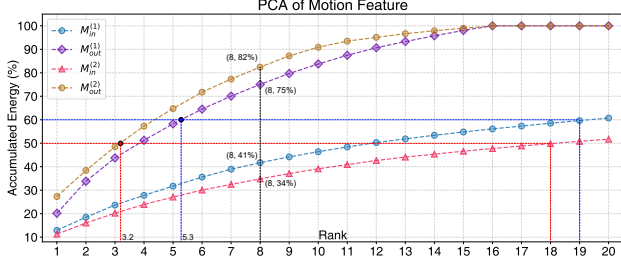


Figure 4. Accumulated energy of the principal components of the motion features, before and after the 1st and 2nd LRR blocks.

The backbone of $h(\cdot)$ generally follows a ResNet-34 structure, except that two newly introduced LRR blocks are inserted at two layers. Each LRR block consists of shallow residual convolution layers and learns K bases for the input motion feature forwarded by the preceding layers. It then generates an output motion feature of rank at most K by subspace projection. Specifically, given an input motion feature $M_{in} \in \mathbb{R}^{H \times W \times C}$, the residual convolution layers convert it into a feature $M_v \in \mathbb{R}^{H \times W \times K}$ of K channels. Then each channel serves as a feature basis $v_k \in \mathbb{R}^{H \times W}$, $k = 1, 2, \dots, K$ after being flattened. Finally, we project M_{in} into the subspace of the feature bases to obtain a low-rank motion feature $M_{out} \in \mathbb{R}^{H \times W \times C}$, *i.e.*

$$M_{out} = V(V^T V)^{-1} V^T \cdot M_{in} \quad (4)$$

where $V = [v_1, v_2, \dots, v_K] \in \mathbb{R}^{H \times W \times K}$. Note that the normalization term $(V^T V)^{-1}$ is required as the feature bases $\{v_k\}$ are not ensured orthogonal.

After the 2nd LRR block, the motion feature computed is forwarded to a group convolution and an adaptive pooling layer, to produce the final 8 weights $\{\alpha_i\}$ for homography flow basis combination. We illustrate the structure of LRR block in Fig. 2, and K is set to 16 in all of our experiments.

3.2. Robust Homography Estimation by LRR

As indicated in Sec. 3.1, a homography flow is of low rank, which means the rank of the motion features through various layers in $h(\cdot)$ should be reduced. Our observation is that, if the rank of the motion feature is reduced, the latent weights for the homography flow bases could be predicted more accurately and easily, where motion outliers are excluded during the rank reduction.

The motion outliers are motions caused by dynamic contents or non-planar depth variations outside the solution space of a single homography. Traditionally, motion outliers are often rejected by RANSAC [16]. In DNN, Zhang *et al.*'s [27] predicted a mask to skip the motion outliers. In this paper, LRR block serves this purpose. It reduces the rank of the motion feature, during which the feature ranks corresponding to the motion outliers are reduced. Because we enforce the network to learn motions

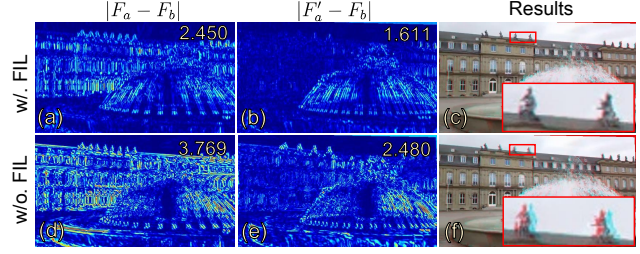


Figure 5. The comparison between with and without warp-equivariance by FIL Loss. Please refer the text for more details.

spanned by the homography bases, any motions outside the subspace are treated as the motion noise. In this way, the non-homography motions can be eliminated automatically during the rank reduction. As a result, a mask predictor as [27] is no longer needed.

As seen in Table 1, with LRR block inserted, our network produces lower error and the overall performance is highly improved compared with [27]. We also analyze the accumulated energy of the principal components for the motion feature M_{in} and M_{out} . As seen in Fig. 4, after the 1st LRR block, the number of principal components (NPC) are reduced from 19 to 5.3 in terms of accumulated energy being 60%. The effectiveness of the 2nd LRR block is more obvious, reducing the NPC from 18 to 3.2 in terms of 50% energy, reflecting the rank of the motion feature is highly reduced. The effectiveness of LRR blocks is also revealed in details in the ablation study in Sec. 4.3.

3.3. Triplet Loss with Feature Warp-Equivariance

With the homography flow H_{ab} estimated, we warp feature map F_a to F'_a and formulate a similar triplet loss without involving an attention mask as in [27], *i.e.*

$$\mathcal{L}_{\mathcal{T}}(I_a, I_b) = \mathcal{L}_{\mathcal{T}}^{ab} = |F'_a - F_b|_1 - |F_a - F_b|_1 \quad (5)$$

The original idea on the triplet loss tries to learn a discriminative feature and an accurate homography simultaneously to well align the input images. Even though it has been demonstrated successful in most cases in [27], it still has the potential to be incorrectly optimized so that $|F_a - F_b|$ is over-maximized while $|F'_a - F_b|$ is still under-minimized, due to the enough DOFs of $f(\cdot)$. To this end, we add a new constraint named “Feature Identity Loss” (FIL) to preserve the warp-equivariance of the learned feature, meaning that the final feature should be approximately identical if we swap the order of warp operation and feature extraction, *i.e.*

$$\mathcal{L}_{\mathcal{W}}(I_a, f, \mathcal{W}_{ab}) = \mathcal{L}_{\mathcal{W}}^{ab} = |\mathcal{W}_{ab}(f(I_a)) - f(\mathcal{W}_{ab}(I_a))|_1 \quad (6)$$

where \mathcal{W}_{ab} is the warp operation by homography flow H_{ab} .

We observe that with this constraint, the optimization of $f(\cdot)$ can be stabilized, improving the accuracy of estimated homography flow. We visualize an example in Fig. 5, where without FIL involved, the triplet loss $\mathcal{L}_{\mathcal{T}}(I_a, I_b)$ is less than

the one optimized with FIL, even though $|F'_a - F_b|$ becomes larger. The reason behind is that the term $|F_a - F_b|$ is much maximized without FIL. As a result, the alignment accuracy is down-graded. We also verify the effectiveness of FIL via an ablation study detailed in Sec. 4.3.

In practice, we also swap the order of I_a and I_b to compute symmetric losses $\mathbf{L}(I_b, I_a)$ and $\mathbf{L}_{\mathcal{W}}(I_b, f, \mathcal{W}_{ab})$, and add a constraint to enforce the homograph flows \mathbf{H}_{ba} and \mathbf{H}_{ab} to be inverse. So, the energy is written as follows,

$$\min_{f,h} (\mathbf{L}_{\mathcal{T}}^{ab} + \mathbf{L}_{\mathcal{T}}^{ba}) + \lambda(\mathbf{L}_{\mathcal{W}}^{ab} + \mathbf{L}_{\mathcal{W}}^{ba}) + \mu|\mathbf{H}_{ab} + \mathbf{H}_{ba}|_2^2 \quad (7)$$

where λ and μ are set to 1.0 and 0.001 in our experiments. We validate the effectiveness of FIL by an ablation study detailed in Sec. 4.3, which shows that it decreases the error at least 8% in average.

4. Experiment

4.1. Dataset and Implementation Details

We evaluate our method using the same dataset as in Zhang *et al.*'s [27], *i.e.* the CA-Unsupervised method. The training set consists of 5 categories of small baseline image pairs in real scenes, including regular (RE), low-texture (LT), low-light (LL), small-foregrounds (SF), and large-foregrounds (LF), each of which contains nearly 160k samples and there are 800k image pairs totally. A randomly selected subset of 4.2k samples is used as the test set, each sample of which contains 6 pairs of labeled matching points for evaluation. Except for the RE, the other 4 scenes are challenging for the homography estimation. For example, the poor image textures of LT and LL scenes limit the feature extraction, and dynamic foregrounds and multi-plane occlusions in SF and LF scenes challenge the background motion identification.

Our network is trained with 360k iterations by the Adam optimizer [13], with parameters $l_r = 10^{-4}$, $\beta_1 = 0.9$, $\beta_2 = 0.999$, $\epsilon = 10^{-8}$. The batch size is set to 16 and the learning rate is reduced by 20% every epoch. It takes nearly 125 hours to complete the entire training with each iteration costing about 1.25s. The implementation is based on PyTorch and the network training is performed on one NVIDIA RTX 2080 Ti. To alleviate the impact of empty boundaries in the warped image, we randomly crop patches of size 320×576 from the original images to serve as input.

4.2. Comparison with Existing Methods

We compare our method with two groups of homography estimation approaches, the DNN-based ones and the feature-based ones. The former group include Supervised [5], Unsupervised [18] and CA-Unsupervised [27] methods, and the latter group includes 14 methods, including 12 combinations of 6 types of features (3 traditional:

SIFT [16] / ORB [19] / BEBLID [21] and 3 DNN-based: LIFT [25] / SOSNet [23] / SuperPoint [6]) and 2 outlier rejection algorithms (RANSAC [7] / MAGSAC [2]), as well as 2 additional customized descriptor matching approaches SuperGlue [20] specifically for SuperPoint [6] only.

Qualitative comparison. Fig. 6 shows the comparison with DNN-based methods. Fig. 6(a) is a scene from RE category with rich textures, which can be aligned accurately by all 4 methods. Fig. 6(b) is from the LL category with repetitive dynamic textures at the river, where the Supervised [5] method fails because it is trained on synthetic data without dynamic contents. The results of the Unsupervised [5] method and the CA-Unsupervised [27] method contain some small errors since both methods cannot reject the dynamic flowing rivers precisely. In contrast, our outlier rejection is achieved via LRR, obtaining accurate principal feature attention compared to the mask of CA-Unsupervised [27].

Our method shows prominent advantage in Fig. 6(c). This scene is from the LT category, where texture quality is extremely poor as in the snow and the sky, and there is a walking man in the foreground making the task much more challenging. In this scene, other methods try to align the moving man since he has more textures than his surrounding areas, while only our method successfully aligns the scene without paying attention to the man, demonstrated by the highlighted pole region.

Fig. 7 further compares our method with all the aforementioned feature-based solutions. In Fig. 7(a), (d) and (g), we validate various feature-based methods in a snow scene, where all of the feature-based methods fail to produce satisfying results, due to either the feature extraction or the foreground interferences. In contrast, our method aligns this scene more accurately.

As for the latter two examples including a low-light and a low-texture one, both of them challenge the feature detection and matching. For instance, in the low-light scene (Fig. 7(b), (e) and (h)), only a small portion of the image contains salient regions. In the sea example (Fig. 7(c), (f) and (i)), it is tough to obtain reliable feature matches on the sea textures. In contrast, our method is naturally more adaptable to the case of insufficient features, benefiting from the pursuit of low-rank features. The qualitative comparison demonstrates our method not only keeps high alignment accuracy in simple scenes but also provides sufficiently reliable results in challenging cases.

Quantitative comparison. We report the quantitative results of various methods in Table 1. For each pair of test images, the average l_2 distances between the warped source points and the target points are considered as the error metric. We report the errors with respect to each scene category. In Table 1, Row 3 ~ 5 are deep homography methods; Row 6 ~ 11 are traditional feature-based methods and

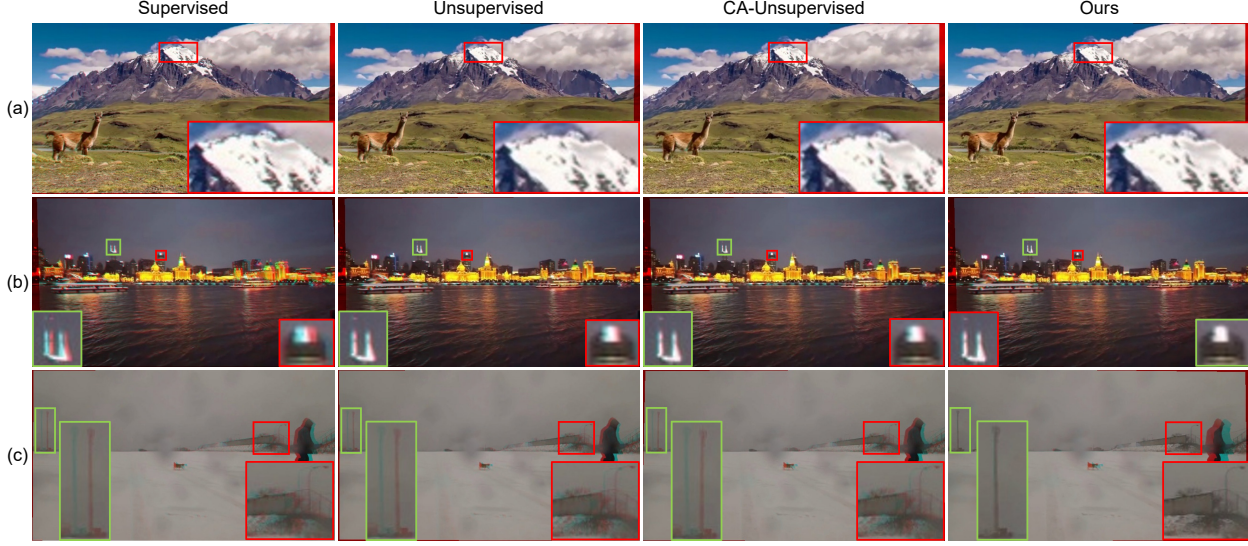


Figure 6. Qualitative comparison with recent DNN-based approaches. Columns 1 ~ 4 are results of supervised [5], Unsupervised [18], CA-Unsupervised [27] and ours. The alignment difficulty in the scenes of 1 ~ 3 Rows increases successively

1)		RE	LT	LL	SF	LF	Avg
2)	$\mathcal{I}_{3 \times 3}$	7.75(+2483.33%)	7.65(+868.35%)	7.21(+930.00%)	7.53(+960.56%)	3.39(+621.28%)	6.70(+963.49%)
3)	Supervised [5]	1.51(+403.33%)	4.48(+467.09%)	2.76(+294.29%)	2.62(+269.01%)	3.00(+538.30%)	2.87(+355.56%)
4)	Unsupervised [18]	0.79(+163.33%)	2.45(+210.13%)	1.48(+111.43%)	1.11(+56.34%)	1.10(+134.04%)	1.39(+120.63%)
5)	CA-Unsupervised [27]	0.73(+143.33%)	1.01(+27.85%)	1.03(+47.14%)	0.92(+29.58%)	0.70(+48.94%)	0.88(+39.68%)
6)	SIFT [16] + RANSAC [7]	0.30(+0.00%)	1.34(+69.62%)	4.03(+475.71%)	0.81(+14.08%)	0.57(+21.28%)	1.41(+123.81%)
7)	SIFT [16] + MAGSAC [2]	0.31(+3.33%)	1.72(+117.72%)	3.39(+384.29%)	0.80(+14.08%)	0.47(+0.00%)	1.34(+112.70%)
8)	ORB [19] + RANSAC [7]	0.85(+183.33%)	2.59(+227.85%)	1.67(+138.57%)	1.10(+54.03%)	1.24(+163.83%)	1.48(+134.92%)
9)	ORB [19] + MAGSAC [2]	0.97(+223.33%)	3.34(+322.78%)	1.58(+125.71%)	1.15(+61.97%)	1.40(+197.87%)	1.69(+168.25%)
10)	BEBLID [21] + RANSAC [7]	0.78(+160.00%)	2.83(+258.23%)	1.38(+97.14%)	1.04(+46.48%)	1.33(+182.98%)	1.47(+133.33%)
11)	BEBLID [21] + MAGSAC [2]	0.94(+213.33%)	3.73(+372.15%)	3.49(+398.57%)	1.17(+64.79%)	1.25(+165.96%)	2.12(+236.51%)
12)	LIFT [25] + RANSAC [7]	0.40(+33.33%)	2.01(+154.43%)	1.14(+62.86%)	0.77(+8.45%)	0.68(+44.68%)	1.00(+58.73%)
13)	LIFT [25] + MAGSAC [2]	0.35(+16.67%)	1.85(+134.18%)	0.96(+37.14%)	0.72(+1.41%)	0.50(+6.38%)	0.88(+39.68%)
14)	SOSNet [23] + RANSAC [7]	0.29(-3.33%)	2.42(+206.33%)	3.71(+430.00%)	0.77(+8.45%)	0.59(+25.53%)	1.56(+147.62%)
15)	SOSNet [23] + MAGSAC [2]	0.30(+0.00%)	3.00(+279.75%)	3.66(+422.86%)	0.87(+22.54%)	0.49(+4.26%)	1.67(+165.08%)
16)	SuperPoint [6] + RANSAC [7]	0.43(+43.33%)	0.85(+7.59%)	0.77(+10.00%)	0.84(+18.31%)	0.80(+70.21%)	0.74(+17.46%)
17)	SuperPoint [6] + MAGSAC [2]	0.45(+50.00%)	0.90(+13.92%)	0.77(+10.00%)	0.76(+7.04%)	0.67(+42.55%)	0.71(+12.70%)
18)	SuperPoint [6] + SG-RAN [20] [7]	0.41(+36.67%)	0.87(+10.13%)	0.72(+2.86%)	0.80(+12.68%)	0.75(+59.57%)	0.71(+12.70%)
19)	SuperPoint [6] + SG-MAG [20] [2]	0.36(+20.00%)	0.79(+0.00%)	0.70(+0.00%)	0.71(+0.00%)	0.70(+48.94%)	0.63(+0.00%)
20)	Ours	0.29(-3.33%)	0.54(-31.65%)	0.65(-7.14%)	0.61(-14.08%)	0.41(-12.77%)	0.50(-20.63%)

Table 1. Comparison of point matching errors between ours and all other methods. SG-RAN and SG-MAG are SuperGlue [20] + RANSAC [7] and SuperGlue [20] + MAGSAC [2] respectively. The percentage in the bracket indicates the improvements over the second best results. Red indicates the best performance and Blue refers to the second best result.

Row 12 ~ 19 are DNN-based feature methods. $\mathcal{I}_{3 \times 3}$ refers to an identity homography, which reflects the original distance between point pairs.

As for the RE scene, the abundant texture provides sufficient high-quality features for homography estimation. So that the feature-based solutions show obvious advantages in this category. Nevertheless, our method and the combination of SOSNet [23] and RANSAC [7] outperform the others and achieve the lowest error of 0.29.

For the low texture (LT) and the low light (LL) scenes, most of the feature-based solutions become less robust due to the difficulty in extracting effective features. In contrast, our method consistently works well. In particular,

the results of the 2nd best method which is constituted by the 3 latest algorithms (SuperPoint [6], SuperGlue [20] and MAGSAC [2]) achieve strong performance. In the scenes containing small (SF) and large (LF) foreground, although sufficient texture features are available, dynamic objects and multi-plane occlusions cause troubles for outlier removal. In our method, objects and multi-plane depth tend to introduce high-rank features in the encoding space, which are abandoned by our low-rank property of LRR blocks. Therefore, our method achieves at least 14.08% and 12.77% lower errors than others on SF and LF, respectively. On the whole, the combination of SuperPoint [6], SuperGlue [20] and MAGSAC [2] produces rather competitive results for



Figure 7. Qualitative comparison with with Feature-based approaches on 3 examples. The combination of various descriptors and outlier elimination methods produced a total of 14 approaches.

all the scenes, but their average errors are still higher than ours by 20.63%.

Robustness evaluation. Furthermore, we evaluate the robustness of all the methods by setting a threshold to judge if a homography matches the marked points. Points with errors lower than the threshold are considered matched inliers, otherwise they are judged as outliers. As such, we report a percentage of matched points overall marked points given

a homography estimation method and a threshold, so that a series of curves are reported in Fig. 8 by setting threshold to 0.1 to 3.0. As seen, our method (the red curve) achieves the highest inlier percentage if the threshold is greater than 0.8, indicating our method can handle intractable cases better than the others. It draws a similar conclusion as Table 1 that our method outperforms others in challenging scenarios, such as LT and LF scenes.

1)	Mask/LRR	Offset/Basis	FIL	RE	LT	LL	SF	LF	Avg
2)	Mask	Offset		0.73(+151.72%)	1.01(+87.04%)	1.03(+58.46%)	0.92(+50.82%)	0.70(+70.73%)	0.88(+76.00%)
3)	Mask	Basis		0.53(+82.76%)	1.05(+94.44%)	1.04(+60.00%)	0.95(+55.74%)	0.56(+36.59%)	0.83(+66.00%)
4)	Mask	Basis	✓	0.45(+55.17%)	1.02(+88.89%)	0.93(+43.08%)	0.96(+57.38%)	0.50(+21.95%)	0.77(+54.00%)
5)	LRR	Basis		0.37(+27.59%)	0.69(+27.78%)	0.75(+15.38%)	0.75(+22.95%)	0.45(+9.76%)	0.60(+20.00%)
6)	LRR	Basis	✓	0.29(+0.00%)	0.54(+0.00%)	0.65(+0.00%)	0.61(+0.00%)	0.41(+0.00%)	0.50(+0.00%)

Table 2. The homography representation solution is chosen in Offset and Basis (homography flow), as well as the outlier rejection module is chosen as Mask [27] or LRR. The FIL as an optional promotion to the effect of the model.

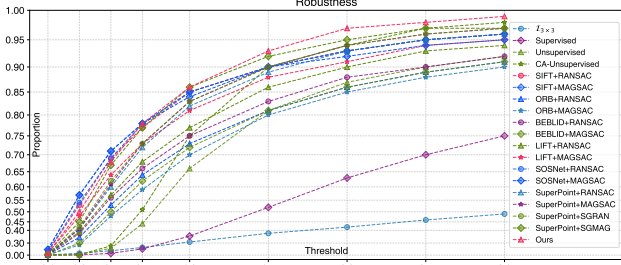


Figure 8. The proportion of inliers in all matching point pairs under various thresholds for all methods. Higher position of curves represent higher robustness.

	0 layer	1 layer	2 layers	3 layers	3 layers*
FIL	0.00	0.14	0.31	0.35	0.11
MSE	0.76	0.69	0.61	0.60	0.50

Table 3. Comparison of point matching errors when $f(\cdot)$ contains a different number of convolution layers. 0 layer means network without $f(\cdot)$. * indicates FIL is involved in training.

4.3. Ablation Studies

We verify the effectiveness of all three contributions by ablation studies, and report the results in Table 2.

Homography flow vs. offsets. The 2nd row of Table 2 shows the result of CA-Unsupervised [27] that adopts offset representation with mask outlier removal. We replace its regression target from the offset to the weights of our homography flow bases, and observe a lower average error and comparable errors in LT, LL and SF scenes being achieved in Row 3. It demonstrates that even for a network not specially designed, the homography flow representation outperforms the old offset solution.

LRR blocks. We further modify the network in Row 3 to our structure (Row 5) by removing the mask module and inserting the LRR blocks into the ResNet-34 homography estimator. As seen, by this replacement, the combination of LRR blocks and homography flow produces a significant advantage, reducing the error by at least about **20%** in all scenarios. A reasonable explanation is that the LRR blocks encourage the utilization of low-rank features for homography estimation, which is conducive to features extraction and outlier rejection.

FIL for warp-equivariance. We also verify the effectiveness of FIL in two structures, *i.e.* the modified CA-

Unsupervised [27] one as in Row 3 and ours as in Row 5, in Table 2. By comparing Row 3 with 4, and Row 5 with 6, we can observe that the average errors are reduced from 0.83 to 0.77 (8% lower) and from 0.60 to 0.50 (17% lower). Especially in the scenes LL and LF, the error reduction is more significant.

To further investigate how FIL improves the optimization, we conduct another experiment by modifying the number of convolutional layers in $f(\cdot)$, from 0 to 3. As seen in Table 3, from $f(\cdot)$ containing 0 to 2 layers without FIL involved in the optimization, the Mean Square Error (MSE) is gradually reduced while the FIL is increased, reflecting the warp-equivariance is damaged. Here “0 layers” means $f(\cdot)$ is removed and photometric loss is used instead. If we continue adding layer to 3, the MSE cannot be decreased showing that the network cannot be consistently optimized, while FIL keeps increasing. If we add FIL to the optimization goal, we can see the MSE is reduced from 0.6 to 0.5 and FIL is decreased significantly from 0.35 to 0.11. This phenomenon reflects that with warp-equivariance preserved, the optimization becomes more stable so that a higher performance can be achieved.

5. Conclusion

We have presented a new deep solution for homography estimation, that involves three new components to improve the performance of previous methods. First, we propose a new representation called homography flow, that replaces the 4 offsets as the regression target. It is achieved by predicting 8 weights to linearly combine 8 pre-computed flow bases. Second, considering homography has only 8 DOFs meaning the motion features through the network should have large rank redundancy, we introduce a LRR block serving as a rank reduction role. With this block, the motion features associated with the dominant homography across two views are retained while the noises are automatically suppressed. We also propose a feature identity loss to enforce the learned image feature warp-equivariant, so that a more stable optimization can be achieved. Extensive experiments demonstrate the effectiveness of all the newly introduced components and experimental results also show that our method significantly outperforms previous methods on benchmark datasets both qualitatively and quantitatively.

References

- [1] Alex, M., and Andrew. Multiple view geometry in computer vision. *Kybernetes*, 1972. 1
- [2] Daniel Barath, Jiri Matas, and Jana Noskova. MAGSAC: marginalizing sample consensus. In *Proc. CVPR*, pages 10197–10205, 2019. 2, 5, 6
- [3] Herbert Bay, Tinne Tuytelaars, and Luc Van Gool. SURF: speeded up robust features. In *Proc. ECCV*, volume 3951, pages 404–417, 2006. 2
- [4] JiaWang Bian, Wen-Yan Lin, Yasuyuki Matsushita, Sai-Kit Yeung, Tan-Dat Nguyen, and Ming-Ming Cheng. Gms: Grid-based motion statistics for fast, ultra-robust feature correspondence. In *Proc. CVPR*, pages 4181–4190, 2017. 2
- [5] Daniel DeTone, Tomasz Malisiewicz, and Andrew Rabinovich. Deep image homography estimation. *arXiv preprint arXiv:1606.03798*, 2016. 1, 2, 5, 6
- [6] Daniel DeTone, Tomasz Malisiewicz, and Andrew Rabinovich. Superpoint: Self-supervised interest point detection and description. In *Proc. CVPRW*, pages 224–236, 2018. 2, 5, 6
- [7] Martin A. Fischler and Robert C. Bolles. Random sample consensus: A paradigm for model fitting with applications to image analysis and automated cartography. *Commun. ACM*, 24(6):381–395, 1981. 1, 2, 5, 6
- [8] Andrew Hartley and Andrew Zisserman. *Multiple view geometry in computer vision* (2. ed.). 2006. 2
- [9] Zisserman A. Hartley, R. *Multiple view geometry in computer vision*. Cambridge University Press, 2003. 1
- [10] Kaiming He, Xiangyu Zhang, Shaoqing Ren, and Jian Sun. Identity mappings in deep residual networks. In *Proc. ECCV*, pages 630–645, 2016. 3
- [11] Paul W. Holland and Roy E. Welsch. Robust regression using iteratively reweighted least-squares. *Communications in Statistics*, 6(9):813–827, 1977. 2
- [12] Max Jaderberg, Karen Simonyan, Andrew Zisserman, and Koray Kavukcuoglu. Spatial transformer networks. In *Proc. NeurIPS*, pages 2017–2025, 2015. 3
- [13] Diederik P. Kingma and Jimmy Ba. Adam: A method for stochastic optimization. In *Proc. ICLR*, 2015. 5
- [14] Hoang Le, Feng Liu, Shu Zhang, and Aseem Agarwala. Deep homography estimation for dynamic scenes. In *Proc. CVPR*, pages 7649–7658, 2020. 1, 2
- [15] Guangcan Liu, Zhouchen Lin, Shuicheng Yan, Ju Sun, Yong Yu, and Yi Ma. Robust recovery of subspace structures by low-rank representation. 35(1):171–184, 2012. 3
- [16] David G. Lowe. Distinctive image features from scale-invariant keypoints. *Int. J. Comput. Vis.*, 60(2):91–110, 2004. 1, 2, 4, 5, 6
- [17] Jiayi Ma, Ji Zhao, Junjun Jiang, Huabing Zhou, and Xiaojie Guo. Locality preserving matching. *International Journal of Computer Vision*, 127(5):512–531, 2019. 2
- [18] Ty Nguyen, Steven W. Chen, Shreyas S. Shivakumar, Camillo Jose Taylor, and Vijay Kumar. Unsupervised deep homography: A fast and robust homography estimation model. *IEEE Robotics Autom. Lett.*, 3(3):2346–2353, 2018. 1, 2, 3, 5, 6
- [19] Ethan Rublee, Vincent Rabaud, Kurt Konolige, and Gary R. Bradski. ORB: an efficient alternative to SIFT or SURF. In *Proc. ICCV*, pages 2564–2571, 2011. 1, 2, 5, 6
- [20] Paul-Edouard Sarlin, Daniel DeTone, Tomasz Malisiewicz, and Andrew Rabinovich. Superglue: Learning feature matching with graph neural networks. In *Proc. CVPR*, pages 4938–4947, 2020. 2, 5, 6
- [21] Iago Suárez, Ghesn Sfeir, José M Buenaposada, and Luis Baumela. Beblid: Boosted efficient binary local image descriptor. *Pattern Recognition Letters*, 133:366–372, 2020. 2, 5, 6
- [22] Chengzhou Tang, Lu Yuan, and Ping Tan. Lsm: Learning subspace minimization for low-level vision. In *Proc. CVPR*, pages 6235–6246, 2020. 3
- [23] Yurun Tian, Xin Yu, Bin Fan, Fuchao Wu, Huub Heijnen, and Vassileios Balntas. Sosnet: Second order similarity regularization for local descriptor learning. In *Proc. CVPR*, pages 11016–11025, 2019. 2, 5, 6
- [24] Jonas Wulff and Michael J Black. Efficient sparse-to-dense optical flow estimation using a learned basis and layers. In *Proc. CVPR*, pages 120–130, 2015. 3
- [25] Kwang Moo Yi, Eduard Trulls, Vincent Lepetit, and Pascal Fua. LIFT: learned invariant feature transform. In *Proc. ECCV*, volume 9910, pages 467–483, 2016. 2, 5, 6
- [26] Jiahui Zhang, Dawei Sun, Zixin Luo, Anbang Yao, Lei Zhou, Tianwei Shen, Yurong Chen, Long Quan, and Hongen Liao. Learning two-view correspondences and geometry using order-aware network. In *Proc. ICCV*, pages 5845–5854, 2019. 2
- [27] Jirong Zhang, Chuan Wang, Shuaicheng Liu, Lanpeng Jia, Nianjin Ye, Jue Wang, Ji Zhou, and Jian Sun. Content-aware unsupervised deep homography estimation. In *Proc. ECCV*, pages 653–669, 2020. 1, 2, 3, 4, 5, 6, 8